Developing Scattering Morphology Resolved Total Internal Reflection Microscopy (SMR-TIRM) for Orientation Detection of Colloidal Ellipsoids

Aidin Rashidi,[#] Sergio Domínguez-Medina,[#] Jiarui Yan, Dmitry S. Efremenko, Alina A. Vasilyeva, Adrian Doicu, Thomas Wriedt, and Christopher L. Wirth*

Read Online

ACCESS | Metrics & More | Article Recommendations | SI Supporting Information

ABSTRACT: Micrometer scale colloidal particles experiencing ∼kT scale interactions and suspended in a fluid are relevant to a broad spectrum of applications. Often, colloidal particles are anisotropic, either by design or by nature. Yet, there are few techniques by which ∼kT scale interactions of anisotropic particles can be measured. Herein, we present the initial development of scattering morphology resolved total internal reflection microscopy (SMR-TIRM). The hypothesis of this work is that the morphology of light scattered by an anisotropic particle from an evanescent wave is a sensitive function of particle orientation. This hypothesis was tested with experiments and simulations mapping the scattered

light from colloidal ellipsoids at systemically varied orientations. Scattering morphologies were first fitted with a two-dimensional (2D) Gaussian surface. The fitted morphology was parameterized by the morphology's orientation angle M_ϕ and aspect ratio M_{AR}. Data from both experiments and simulations show M_ϕ to be a function of the particle azimuthal angle, while M_{AR} was a sensitive function of the polar angle. This analysis shows that both azimuthal and polar angles of a colloidal ellipsoid could be resolved from scattering morphology as well or better than using bright-field microscopy. The integrated scattering intensity, which will be used for determining the separation distance, was also found to be a sensitive function of particle orientation. A procedure for interpreting these confounding effects was developed that in principle would uniquely determine the separation distance, the azimuthal angle, and the polar angle. Tracking these three quantities is necessary for calculating the potential energy landscape sampled by a colloidal ellipsoid.
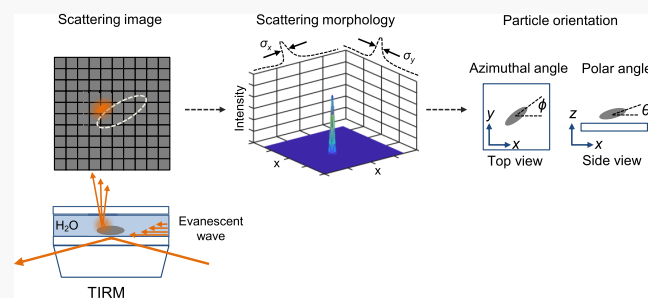
INTRODUCTION

Colloidal particles near a boundary sample a potential energy landscape that depends upon the local physicochemical properties, such as salinity, pH, suspended or adsorbed solutes, and bound surface charge. These ∼kT scale surface interactions play a key role in nearly every application in which suspended particles are found, in particular, when particles deposit onto a substrate or interact with neighbors.[1−6] The design, processing, and application of fluids containing suspended colloidal particles critically depend upon characterizing these ∼kT scale surface interactions. Further, observing the interaction and the deposition of colloids on a substrate has been used to screen antifouling coatings[7] and evaluate the diseased state of red blood cells.[8] A variety of techniques, including the atomic force microscope (AFM), surface force apparatus (SFA), and total internal reflection microscopy (TIRM), were developed and widely adopted to measure surface interactions.[9,10] TIRM is particularly well suited for measuring weak ∼kT scale interactions because of the technique's sensitivity.[11]

TIRM works by tracking the Brownian fluctuations of a particle with the intensity of light scattered from an evanescent wave.[12] Fluctuations normal to the boundary are tracked. Assuming that the particle samples a Boltzmann distribution of height allows one to assemble the potential energy profile from many independent observations. In addition to conservative interactions,[13−17] TIRM has also been used to measure nonconservative hydrodynamic interactions[18] and the response of a particle to an electric field.[19,20] A TIRM apparatus nominally includes an upright microscope with a laser beam incident to the fluid cell.[12] Although the region of interest (ROI) is initially identified in bright field, a TIRM measurement is conducted in the absence of backlight, with the only
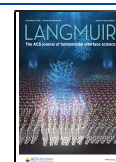
light in the ROI scattered by the particle itself from the evanescent field, becoming a propagating wave that can reach the detector. One significant advance in conducting TIRM was in the implementation of a camera as a sensor for collecting scattered light, rather than a photomultiplier tube (PMT).[21] Using a camera as the sensor, paired with appropriate image processing, facilitates measurement of multiple particles at the same time in a single ROI.[22] Parallelizing the measurement allows for ensembles of particles to be observed and certain multibody effects to be probed.[21] TIRM is capable of measuring $\sim kT$ scale interactions because of the exquisite sensitivity of light scattered from the particle as a function of separation distance. A typical TIRM experiment will nominally collect 100 000 observations of a single particle with intervals of ~ 10 ms and achieve a vertical spatial resolution of ~ 1 nm. Such spatial and temporal sensitivity gives TIRM advantages in certain situations over other techniques that require three-dimensional (3D) stacking of confocal images to track particles.[23] Recent advances in optical microscopy have demonstrated measurements of the orientation of anisotropic particles in three dimensions using wide-field images. For instance, differential interference contrast (DIC) microscopy[24] and total internal reflection scattering microscopy (TIRS)[25,26] have shown orientation sensing of nanometer-sized gold nanorods with subdegree angular precision. In addition, surface plasmon resonance microscopy has been used to track the 3D rotation of unlabeled rodlike particles during photocatalysis.[27] While there is no question of the remarkable success of these techniques for orientation sensing of anisotropic particles, these fall short at providing information on the particle–surface separation distance, which is ultimately extracted from TIRM experiments to construct potential energy landscapes.

Novel anisotropic particles, spurred by new fabrication routes developed over the past 2 decades,[28] now present a fresh challenge for tracking interactions and dynamics but also specifically for TIRM. The essential feature of classic TIRM is that an integrated scattering signal is obtained to track fluctuations in height. However, one would expect that anisotropic particles about the size or larger than the wavelength of light would scatter as a function of not only position but also orientation.[29] Collecting a single intensity value for a given observation in time, as is done in classic TIRM, convolutes the signal in a way that both position and orientation information cannot be obtained. Moreover, this orientation information would be critical to tracking dynamics and calculating the potential energy landscape sampled by an anisotropic particle. Previous work has shown that observations of both position and orientation can be analyzed to assemble potential energy landscapes,[30] thereby providing a framework for assembling such a landscape for an anisotropic particle. One particular example in which an interaction landscape for an anisotropic particle would be useful is for the design of diagnostic tools for determining the diseased state of a red blood cell, which is anisotropic, as it interacts with a boundary.

Herein, we summarize the initial development of scattering morphology resolved total internal reflection microscopy (SMR-TIRM). The essence of SMR-TIRM is in analyzing the morphology, rather than the integrated intensity, of light scattered from a particle interacting with an evanescent wave. We systematically mapped scattered light from particles of known aspect ratio, orientation, and position. This strategy was carried out with both experiments and simulation,[31] allowing us to determine the dependence of morphology at these various conditions. We found that both the intensity and morphology of light scattered by an ellipsoid were dependent upon particle orientation in both the azimuthal and polar angles. Results presented herein are the first step toward the direct measurement of energy landscapes of anisotropic particles.

■ MATERIALS AND METHODS

Preparation of Ellipsoidal Particles by Uniaxial Stretching. Ellipsoidal particles of different aspect ratios (AR = 1.7 ± 0.1 and 3.0 ± 0.3) were fabricated by uniaxial stretching of polystyrene spherical beads (PS, Molecular Probes, lot# 1964358, 4 wt % suspension, initial diameter = 4.9 ± 0.3 μm), following a mechanical deformation method developed by Ho et al.[32] After stretching, the resulting ellipsoidal particles had major axes $(2a)$ = 7.1 ± 0.5 and 11.3 ± 0.9 μm and minor axes $(2b)$ = 4.2 ± 0.2 and 3.8 ± 0.5 μm. Similar spheroidal latex beads have been used by Doicu et al. in light scattering experiments.[33] In brief, 2 g of the polystyrene bead suspension was dispersed into an aqueous poly(vinyl alcohol) (PVA, POVAL 40-88 Kuraray poly(vinyl alcohol)) solution, containing 7.5 g of PVA and 300 g of ultrapure water. After homogenization for 24 h, the mixture was slowly poured on a square poly(vinylidene difluoride) (PVDF) tray (25 cm × 25 cm) and further settled to dry into a thin film at room temperature for approximately 2 days. The film was carefully recovered from the PVDF surface and cut into squares of 10 cm × 10 cm, where 1 cm × 1 cm grids were drawn to track the uniformity of the film stretching procedure. A single square was held between the two clamps of a custom-made automatic uniaxial stretching machine. The stretching was done at 130 °C after an equilibration time of 5 min. Because this temperature is above the glass-transition temperature of polystyrene, the beads plastically deform and stretch. This procedure is performed at two different draw ratios to produce ellipsoids with two different aspect ratios. Following the stretching process, sections of the square films were dissolved by stirring in a mixture of isopropyl alcohol (IPA) and ultrapure water (3:7 v/v) for 12 h. The suspension was then centrifuged and redispersed in the same IPA–water solution three times to remove PVA. Afterward, several cycles of centrifugation and redispersion were repeated in ultrapure water to further purify the sample. Finally, the washed ellipsoids were dispersed in a KCl solution at a concentration of 10^{-5} M and stored in a refrigerator at ~ 4 °C. A picture of the uniaxial stretching machine and results of size measurements of the two samples of ellipsoids by scanning electron microscopy (SEM) are shown in Figure S1.

Total Internal Reflection Microscopy (TIRM) of Ellipsoidal Particles. The total internal reflection microscopy (TIRM) setup is based on an upright microscope system (Olympus BX51WI). The output of a 633 nm laser (PLM-633.0-PMF, NECSEL Co.) is passed through a single-mode 1 m optical fiber (NECSEL), which is coupled to an aspherical collimator (CFC-8X-A, f = 7.5 mm, Thorlabs). The collimator is directly attached to a custom-built aluminum mount that holds a linear polarizer (set to p-polarization, FBR-LPVIS 500–720 nm, Thorlabs) and a custom-made trapezoidal prism (BK7 glass, width: 25 mm, length: 50 mm at the larger facet) with diagonal sides of 68 and 75°. For experiments and simulations described herein, the angle of incidence was 75°. This is larger than the critical angle required to achieve total internal reflection in a glass–water (n_1 = 1.515, n_2 = 1.33) interface (θ_c = 61°), resulting in an evanescent wave that travels parallel to the glass surface and which intensity decays exponentially in the water medium. The laser power was set to 20 mW using an automated computer control (Raman Boxx, NECSEL). The sample was placed inside a microfluidic cell made of a 2 mm thick microscope slide at the bottom and a thin cover slide (Fisher Scientific) at the top. Vacuum grease (Dow Corning) was used between the slides and the gasket to prevent leaks. The microfluidic cell was placed on top of the prism using refractive index matching oil (Resolve, Thermo Scientific, n = 1.515).
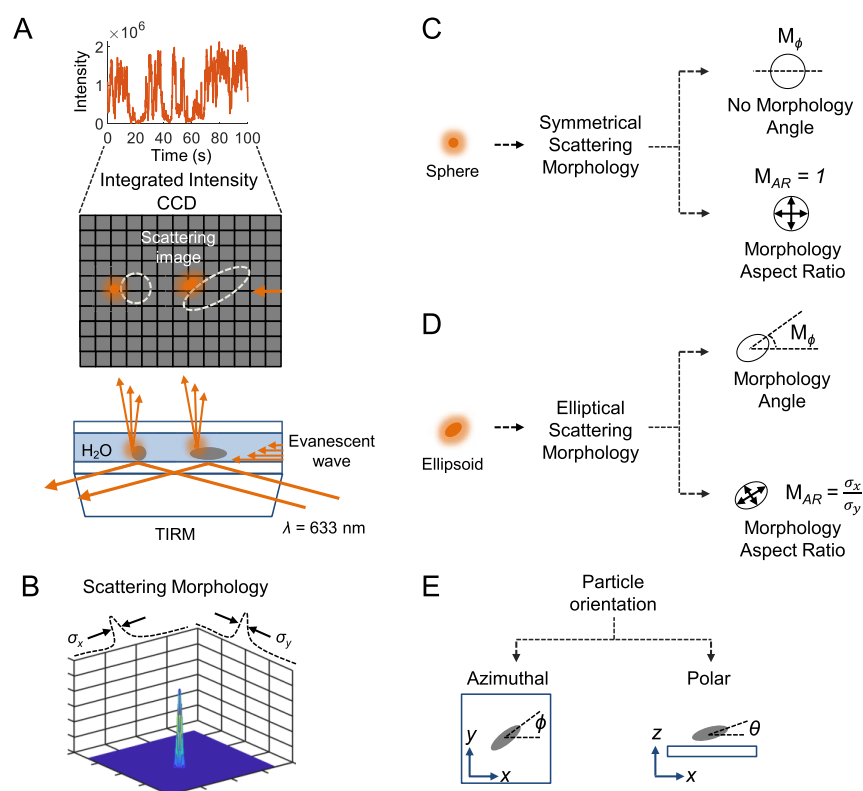
Figure 1. Scattering morphology resolved total internal reflection microscopy (SMR-TIRM). (A) Simplified diagram of the TIRM setup. The integrated scattering intensity is obtained from the sum of the intensity of the individual camera pixels at a given frame. (B) Scattering morphology is extracted by fitting a 2D Gaussian function to the scattering image. (C) Spherical particle produces a symmetrical scattering morphology, with no measurable morphology angle M_ϕ because the morphology aspect ratio (M_{AR}) is equal to 1. (D) Ellipsoidal particle produces an elliptical scattering morphology, from which the morphology angle M_ϕ and morphology aspect ratio (M_{AR}) can be measured. (E) Diagrams showing the azimuthal ϕ and polar θ angles of an ellipsoidal particle deposited on a substrate.

Before assembly, the microscope slides were previously washed in acetone (HPLC grade, Alfa Aesar), ethanol (200 proof anhydrous, Decon Laboratories), and water, followed by drying with tetrafluoroethane (MS-222N, Miller Stephenson). The purified polystyrene ellipsoids were dispersed in a 10 mM NaCl solution ($n = 1.33$, $T = 23$ °C), sonicated for 30 min, and injected inside the microfluidic cell, which has a volume of ~20 μm. This electrolyte concentration ensured charge screening of the negatively charged particles, allowing them to deposit onto the negatively charged glass surface in about 30 min. The particle concentration was kept low enough to prevent scattering interference from neighboring particles within the region of interest used for individual particle measurements (101×101 pixels^2).

The scattered light of isolated ellipsoids attached to the glass surface was collected with a 40× microscope objective directly above the sample (LUCPLFLN40X, NA = 0.6, Olympus). The light was then passed through a demagnifying adapter (0.63×) and collected by a digital air-cooled CCD camera (Hamamatsu ORCA-R^2). The camera was operated with a control unit and computer software provided by the manufacturer (cellSens, Olympus). The images were acquired at full resolution (1344×1024 pixels^2) with an acquisition time of 10 ms and an 8-bit depth, unless indicated otherwise. The images were saved in uncompressed JPEG format. A mechanical stage was used to find the region illuminated by the evanescent wave to align the sample with the camera. In addition to TIRM illumination, the ellipsoids were also separately imaged with white light from a halogen lamp (12 V, 100 W maximum power, Phillips) from the back of the sample (i.e. bright-field imaging). To minimize the effects of sample heating, the power was reduced using a controller to ~25 W. In addition, the lamp was used without a condenser and only turned on to locate the ellipsoids on the sample (<30 s). These back-

illuminated images were used to measure the particle azimuthal angle (ϕ), using an automated routine in ImageJ.

T-Matrix Simulations of Scattering Images of Ellipsoidal Particles under Evanescent Wave Scattering. A light scattering model for TIRM was used to simulate the scattering of an ellipsoidal particle of arbitrary orientation placed in an evanescent field near a plane surface, as described in detail elsewhere.[34] The light scattering model especially includes the scattering interactions between the particle and the plane surface. In brief, the scattering problem is solved by relating the incident and scattered field coefficients in the framework of the T-matrix method,[35,36] where the matrix elements are calculated by matching the boundary conditions for solutions of Maxwell equations.[34] Then, the reflection matrix containing the elements of the scattered field by the surface is computed by using the integral representation of the spherical vector wave functions, which are then rotated using the rotation addition theorem to handle an arbitrary particle orientation. Finally, the imaging of the scattered field is obtained by simulating the microscope optics of a 4-f imaging system, which is achieved by computing the focus field distribution using the Debye diffraction integral.[37]

The simulation program is written in a modular form based on the original FORTRAN code[38] and requires user input in a set of physical parameters related to the particle–substrate geometry and materials, the optical excitation and incidence angle, numerical convergence of the T-matrix method, and the scattering imaging geometry. These parameters were chosen to match the TIRM experiment and are summarized in Table S1. The code produces several output files, which include the results of the convergence analysis of the T-matrix method, the elements of the T-matrix itself, the differential scattering cross sections, the integrated intensity, and the values and coordinates of the focus field distribution that are used to build a scattering image. On average, each scattering image took 18 min of computation time
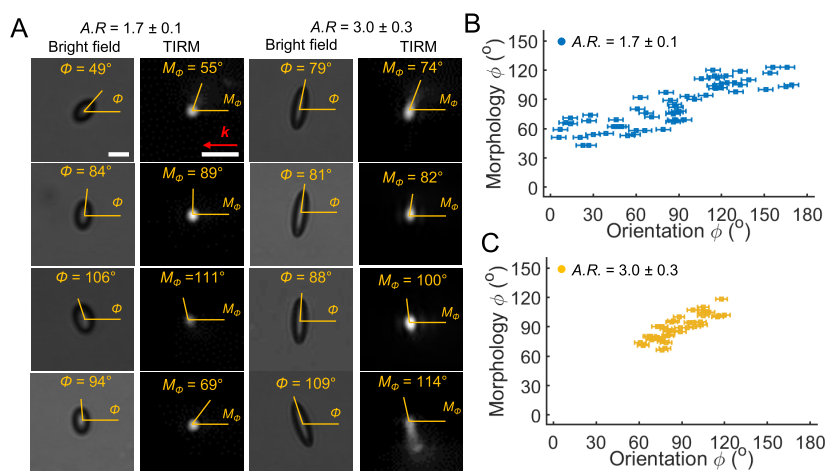
Figure 2. Azimuthal orientation sensing of SMR-TIRM images. (A) Experimental scattering images of ellipsoidal particles (AR = 1.7 and 3.0) parallel to a substrate, for bright field (θ_{inc} = 0°) and TIRM (θ_{inc} = 75°). The uncertainty in ϕ in the bright-field images is ±5 and ±4° for AR = 1.7 and 3.0, respectively. The direction of propagation of the evanescent wave is indicated with the k-vector. Scale bars = 5 μm for all images. (B) Measurements of the scattering morphology angle M_ϕ obtained from TIRM images as a function of the azimuthal particle orientation ϕ, for AR = 1.7. (C) Same plot as in panel (B) for ellipsoids with AR = 3.0.

using an Intel i7-9700 processor (3.0 GHz). Note that the particle–surface separation distance d was set to 0.1 μm, well inside the range of the evanescence field. While we expect the deposited particles in the experiment to be in contact with the surface, the separation distance only affected the scattering intensity but not the scattering morphology of the images produced. The routine to compute the light scattering by an arbitrarily shaped dielectric particle near a surface is available on the Scattport.org website.[39] While this manuscript only shows two examples of prolate spheroids with low and high aspect ratios, the routine can also be applied to compute the scattering morphology of oblate spheroids.

Analysis of the Scattering Morphology by Using a Two-Dimensional (2D) Gaussian Function. Experimental and simulated scattering images of ellipsoidal particles were analyzed by fitting a 2D Gaussian function to the centroid of the image, by customizing an automated fitting routine in MATLAB.[40] The scattering morphology is then extracted from two key parameters: first, the morphology angle M_ϕ, which is the angle of rotation of the major axis of the 2D Gaussian fit, measured counterclockwise from a horizontal reference. Second, the morphology aspect ratio M_{AR}, which is the ratio of the major σ_x and minor σ_y axes of the 2D Gaussian fit and which measures the ellipticity of the scattering morphology. Hence, an M_{AR} = 1 represents a radial symmetrical scattering morphology, while M_{AR} > 1 represents an elliptical morphology. For calibration purposes, the scattering morphology of experimental and simulated images is analyzed as a function of the particle azimuthal angle ϕ for a given aspect ratio, at a polar angle θ = 0° (i.e. an ellipsoid parallel to the surface rotating in the azimuthal plane). Constructing this calibration curve allows M_ϕ to be used as a reporter of the azimuthal angle ϕ in experimental TIRM images, which is then compared with the azimuthal particle orientation observed by bright-field illumination, to assess the viability of this orientation-sensing method. Likewise, M_{AR} is also measured as a function of ϕ for θ = 0° in simulation images. However, this analysis is further used to explore the effect of small variations in θ in simulated images, as this can occur during particle deposition of ellipsoids (i.e. ellipsoids that are not perfectly horizontal with respect to the surface). This is explained in further detail in the Results and Discussion section of this paper.

RESULTS AND DISCUSSION

Under evanescent wave illumination, the scattering of an ellipsoidal particle does not only depend on the particle–substrate separation distance but also depend on its orientation with respect to the light source (i.e. the k-vector of the

evanescent wave). The use of anisotropic particles in a typical TIRM experiment, in which the integrated intensity is collected, has been unfeasible due to anisotropic scattering. In the conventional TIRM experiment, the Brownian fluctuations of a spherical particle diffusing near a surface are observed through the light the particle scatters in an evanescent wave. The geometry of the illumination is such that the exponential decay of the evanescent wave intensity is perpendicular to the surface, with a penetration depth (β^{-1}) that depends on the laser wavelength λ_0, its incidence angle (θ_{inc}), and the refractive indices of the surface (n_1) and diffusive media (n_2)

$$\beta = \frac{4\pi}{\lambda_0}\sqrt{(n_1 \sin(\theta_{inc}))^2 - n_2^2} \tag{1}$$

The intensity of the scattered light by the particle (I_{sc}) also follows the exponential decay of the evanescence wave

$$I_{sc}(h) = I_0 \exp(-\beta h) \tag{2}$$

where I_0 is the particle intensity at h = 0. Because typically β^{-1} ~ 100 nm, the height (h) fluctuations of the particle can be tracked with subdiffraction resolution, as variations of ~1% in I_{sc} can be measured with modern photodetectors. However, it should be noted that eq 2 can only be used with spherical particles, as fluctuations in their isotropic scattering must exclusively arise due to changes in h.

Figure 1 summarizes the operating principle of scattering morphology resolved TIRM, which aims to extract the particle orientation from the scattering image (i.e. scattering "morphology") of a particle near a boundary under evanescent wave illumination. For a spherical particle, the scattering morphology is symmetrical. Integration of the signal contains the information required to interpret intensity fluctuations as changes in height using eqs 1 and 2. On the other hand, the scattering morphology of ellipsoidal particles has an elliptical pattern and hence can be characterized by implementing a 2D Gaussian fit on the scattering images. As explained in the Analysis of the Scattering Morphology by Using a Two-Dimensional (2D) Gaussian Function section, we then extract
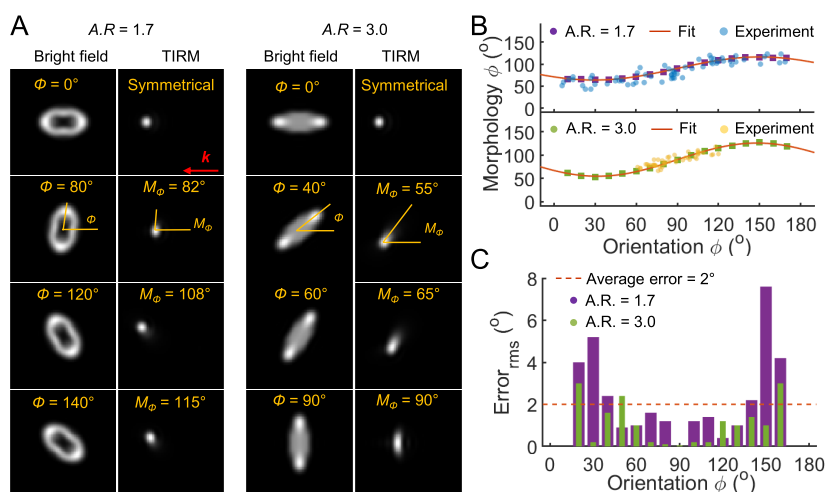
Figure 3. Azimuthal orientation sensing of simulated SMR-TIRM images. (A) Simulated scattering images of ellipsoidal particles (AR = 1.7 and 3.0) parallel to a substrate, for bright field (θ_{inc} = 0°) and TIRM (θ_{inc} = 75°). The direction of propagation of the evanescent wave is indicated by the k-vector. The halos observed in the bright-field images for AR = 1.7 are likely due to a diffraction pattern. (B) Measurements of the scattering morphology angle M_ϕ as a function of the azimuthal particle orientation ϕ, for AR = 1.7 (top panel) and 3.0 (bottom panel). The simulated data is fit to an empirical sinusoidal equation. The experimental data is overlaid for comparison. (C) Root-mean-squared (RMS) error of ϕ obtained by this model, broken down in 10° steps.

the morphology angle (M_ϕ) and morphology aspect ratio (M_{AR}) from the Gaussian fit.

We applied this SMR-TIRM methodology to ellipsoidal particles randomly oriented in the azimuthal angle and deposited (separation distance, h = 0) on a substrate. The following three sections summarize our results and discussion: (A) measuring the particle azimuthal orientation (in-plane, ϕ) using the morphology angle M_ϕ, (B) simulating the effect of variations in the particle polar angle (out of plane, θ) using the morphology aspect ratio (M_{AR}), and (C) evaluating the effect of the particle orientation in the scattering intensity, thus paving the way toward the use of ellipsoidal particles as TIRM probes for surface interactions.

(A). Measuring the Particle Azimuthal Orientation (In-Plane, ϕ) Using the Morphology Angle M$_\phi$. The azimuthal orientation of an ellipsoidal particle in a plane (ϕ) was obtained with SMR-TIRM, by measuring M_ϕ from the light scattered by the particle under evanescent wave excitation. To establish a relation between ϕ and M_ϕ, we first analyzed the scattering morphology of 108 individual ellipsoids deposited on a glass surface at random orientations. Figure 2A shows a representative set of these images, in which each pair corresponds to the same particle illuminated with bright-field and TIRM excitation, as indicated at the top of each column. Approximately half of the collected images corresponded to ellipsoids of AR = 1.7 and the other half to AR = 3.0. Figure 2B shows the measured values of M_ϕ as a function of ϕ obtained from the scattering morphology of 63 ellipsoids of AR = 1.7. Similarly, Figure 2C shows the measured values of M_ϕ as a function of ϕ obtained from the scattering morphology of 45 ellipsoids of AR = 3.0. However, for these high-aspect-ratio ellipsoids, only angles between 61 and 115° were observed by TIRM with enough contrast with the current setup, as the scattering intensity decreased substantially outside this range of angles. Additional experimental bright-field and TIRM images are shown in Figure S2. Presumably, some particle orientations are more efficient at scattering light than others, an effect that seems to be enhanced for particles with higher aspect ratio. The relation-

ship between M_ϕ and ϕ will be explored next by simulations of the scattering morphology, with the goal of finding an expression that can be used to link the morphology angle M_ϕ (i.e., the observable) with the azimuthal orientation ϕ (i.e. the unknown parameter) of the ellipsoid.

Simulated bright-field and TIRM images were produced by the T-matrix method described in the Materials and Methods section, for a range of ϕ between 0 and 180° with 10° steps. Figure 3A shows the simulated scattering images for eight different angles, for ellipsoids of AR = 1.7 and 3.0, as indicated in the top of the columns. Each pair of images corresponds to the same ellipsoid illuminated under bright-field (θ_{inc} = 0°) and TIRM (θ_{inc} = 75°) excitation, as was done in the experiment. M_ϕ was then obtained from the TIRM images using the 2D Gaussian method. One important thing to note is that the simulations predict a symmetrical scattering morphology when ϕ = 0 and 180°. Thus, M_ϕ is not defined at these angles.

We confirmed that M_ϕ is dependent on ϕ by constructing a curve between the two values. Figure 3B shows the relation between M_ϕ and ϕ for the scattering morphology of the simulated TIRM images shown in Figure 3A. The experimental data from Figure 2A is overlaid as comparison. While the observed agreement between simulations and experiments is promising, we also note that the simulated data predicts a nonlinear relation between M_ϕ and ϕ. Thus, we fitted the simulated data with an empirical sinusoidal fit of the form M_ϕ = $P_1 \cdot \cos(\omega \cdot \phi)$ + $P_2 \cdot \sin(\omega \cdot \phi)$ + P_3. This would imply a periodicity for the relation between M_ϕ and ϕ that can be described by a fundamental angular frequency ω. Identical values for ω were found for the low- and high-aspect-ratio ellipsoids (ω = 0.026 ± 0.001 or a period $T = \frac{2\pi}{\omega}$ = 240 ± 10°). We suspect that this sinusoidal feature was not readily observed in Figure 2B,C because of noise in the experimental images. In the future, more sensitive imaging would aid in the elucidation of the underlying relation between these two parameters. What is important for our purpose is that this sinusoidal fit can be used to determine the azimuthal orientation of the particle from the observable M_ϕ in the
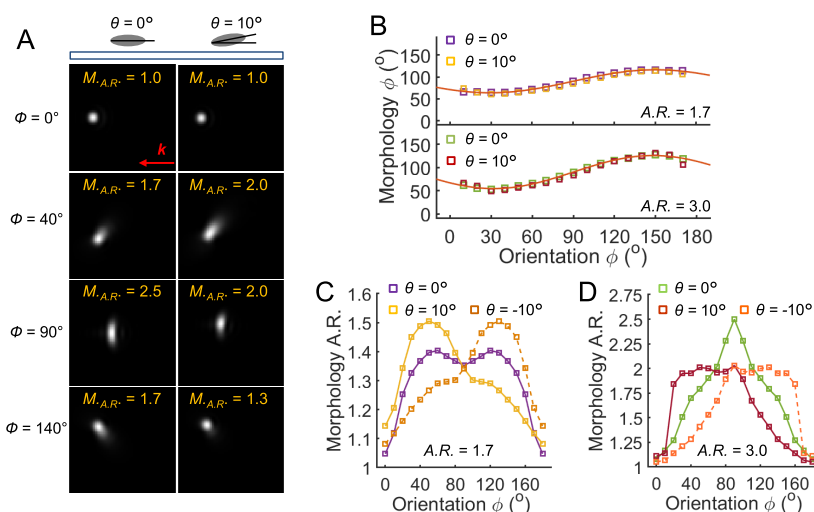
Figure 4. Effect of a small tilt in the polar angle in simulated SMR-TIRM images. (A) Representative simulated TIRM images of ellipsoids with AR = 3.0 at θ = 0 and 10°. The morphology aspect ratio (M_{AR}) is indicated in each TIRM image. (B) Measurements of the scattering morphology angle M_ϕ as a function of the azimuthal particle orientation ϕ for AR = 1.7 (top panel) and 3.0 (bottom panel), where θ = 0 and 10° are overlaid with different colors. The sinusoidal fit is shown with a solid red line. (C) Effect of M_{AR} with the particle azimuthal orientation ϕ, where θ = 0, 10, and −10° are shown with different colors, for an ellipsoid of AR = 1.7. (D) Same plot as in (C) for an ellipsoid of AR = 3.0.

absence of backlight. Note that the uncertainty in the measurement of ϕ expected due to the "blurring" of diffraction in our bright-field images was estimated to be ∼5° (Figure S3), which will be compared next to the angular error in ϕ obtained from applying the sinusoidal fit to the simulated data.

The angular errors obtained by applying this empirical sinusoidal relation on the simulated data are equal or smaller than the estimated uncertainty in ϕ in our bright-field images. Figure 3C shows the RMS error of applying the sinusoidal fit to obtain ϕ from the simulated TIRM images. Because the real ϕ was an input in the simulations, the RMS errors are calculated to these values and can be broken down for every 10° step. The average RMS error across all orientations tested was found to be 2°, which is lower than the ±5° estimate from bright-field images. Interestingly, this implies that the upper limit (i.e., best-case scenario) of the angular resolution of this SMR-TIRM approach is better than orientation sensing by bright-field imaging.

(B). Simulating the Effect of Variations of the Particle Polar Angle. Detecting small variations in the particle polar angle through bright-field images collected from the top (or bottom) of the sample is particularly challenging. The angular resolution for detecting changes in the polar angle is more limited than for those that occur in the azimuthal plane. An estimate of the angular polar resolution can be calculated by considering the length of the projection of the major axis of the ellipsoid when it is tilted out of plane. For this tilt to be perceived in a bright-field image, the change in projected length has to be at least equal to the lateral resolution of the microscope system used. In our case, for λ = 0.633 μm and numerical aperture NA = 0.6, we calculate our lateral resolution to be $0.61\frac{\lambda}{NA}$ = 0.643 μm. Thus, the minimum change in the projection of the major axis ($2a$) of the particle when tilting out of plane has to be at least equal to this value. For ellipsoids with $2a$ = 7.1 and 11.3 μm (as those used in the experiment), the minimum projections that can be measured are ($2a$ − 0.643 μm) and hence equal to 6.5 and 10.7 μm, respectively. The minimum changes in the polar angle that can be detected with bright-field imaging are then

$\cos^{-1}\left(\frac{(2a - 0.643\ \mu m)}{2a}\right)$, equal to ∼25 and 20° for the low- and high-aspect-ratio particles imaged in the experiment, respectively (Figure S4). It should be noted that these values do not consider the effect of defocusing, which would decrease the angular resolution even further. Then, we proceeded to test how the parameters of SMR-TIRM are affected by small variations in the polar angle that would be otherwise undetectable with bright-field imaging.

We simulated a small out-of-plane tilt of 10° to investigate the effect in SMR-TIRM of a small change in the polar angle. First, this served to evaluate the robustness of the detection method for measuring the azimuthal angle. Second, these calculations were used to assess whether the morphology aspect ratio could be used to detect variations in the polar angle. Figure 4A shows the simulated TIRM scattering images of ellipsoids of AR = 3.0 at four different azimuthal orientations ϕ. The diagram above the images shows a side view of the ellipsoid at θ = 0° (i.e., major axis parallel to the substrate) and 10°. Each image was then analyzed by the 2D Gaussian method, from which M_ϕ and M_{AR} were extracted as a function of ϕ for different θ.

The ability to detect the azimuthal orientation ϕ of an ellipsoid using SMR-TIRM is not affected by small changes in the polar angle θ. Figure 4B shows the relation between M_ϕ and ϕ for θ = 0 and 10°, in ellipsoids of AR = 1.7 and 3.0, respectively. It can be readily noticed that a small change of θ = 10° does not affect the underlying relation between ϕ and M_ϕ. If a sinusoidal calibration were to be used to later extract the particle orientation by only measuring M_ϕ, the results would be identical as the fits overlay each other. Therefore, the noise observed in the experimental data shown in Figure 3B is not a result of small variations in θ that could have occurred when these were deposited on the surface.

In contrast, the aspect ratio of the scattering morphology M_{AR} is strongly affected by the particle polar angle. Figure 4C,D shows the values of M_{AR} for a full rotation of ϕ between 0 and 180°, for ellipsoids AR = 1.7 and 3.0, respectively. For the ellipsoid with a lower aspect ratio, the highest values of

M_{AR} (i.e., the most elliptical scattering morphologies) are observed at $\phi = 60$ and $120°$ and the lowest at $\phi = 0$ and $180°$ (i.e., the most symmetrical morphology). For the ellipsoid with a higher aspect ratio, the highest value of M_{AR} is at $\phi = 90°$, when the k-vector and the major semiaxis are orthogonal. Similar to the ellipsoid of low aspect ratio, the values of M_{AR} decrease to 1 as ϕ approaches 0 and $180°$. For both types of ellipsoids, the trends are symmetric at $90°$ when $\theta = 0°$, as each value of M_{AR} is identical for every $2 \cdot (\phi - 90°)$, when $\phi \neq 90°$. Hence, unlike M_ϕ, M_{AR} cannot be used by itself to unambiguously identify ϕ.

However, these data show the morphology aspect ratio M_{AR} to be exquisitely sensitive to changes in the polar angle θ for a wide range of ϕ. Figure 4C,D also shows the values of M_{AR} for $\theta = 10$ and $-10°$ for the same simulated ellipsoids. The relative change in M_{AR} varies with ϕ and with the particle AR. For instance, the largest relative change in M_{AR} is -45% for the high-aspect-ratio ellipsoid at $\phi = 20°$ and -11% for the low-aspect-ratio ellipsoid at $\phi = 140°$. A summary of the relative changes in M_{AR} as a function of ϕ can be found in Tables S2 and S3. These results suggest that only in small regions near polar orientations of 0, 90, and $180°$ would M_{AR} be unable to detect the polar orientation. Recall that such small changes in θ would be undetectable by analyzing the projection of bright-field images, as the out-of-plane angular resolution is between 20 and $25°$. This is promising for the development of SMR-TIRM to potentially achieve 3D orientation tracking of ellipsoidal particles, by using a combination of M_ϕ and M_{AR} in a (ϕ, θ) space.

In addition to the measurement of angular position, measurement of fluctuations in height is also an essential part of a TIRM experiment. One would expect the morphology intensity to be the main reporter of separation distance for SMR-TIRM, in particular, at a fixed orientation.[31] Herein, we now proceed to evaluate how orientation affects the scattered light intensity by the ellipsoids in an evanescent field.

(C). Evaluating the Effect of the Particle Orientation in the Scattering Intensity. In a classic TIRM experiment with a spherical particle probe, intensity fluctuations arise solely from changes in separation distance. These fluctuations are tracked to construct a potential energy landscape of the particle−surface interaction. However, for anisotropic particles, orientational changes also affect the integrated intensity. Deconvoluting these quantities, namely, separation distance and orientation, is required for conducting SMR-TIRM and obtaining the potential energy landscape of an anisotropic particle interacting with a surface.

Along with the simulated scattering images of ellipsoids under evanescent wave illumination, the integrated scattering intensity was computed by modeling a similar imaging system as in the experimental setup (NA = 0.6; other relevant parameters can be found in Table S1). Note that these simulations assume that all particles are illuminated with the same evanescent wave intensity in the x and y planes, which would not be the case for an experimental evanescent field due to the laser spatial distribution in x, y. However, regardless of the particle lateral position within the evanescent wave, the integrated scattering intensity is expected to decay exponentially as in eq 2. This is shown in Figure 5A, where the integrated scattering intensity by a particle at a fixed orientation decays exponentially with separation distance. Here, the integrated intensity is calculated relative to the
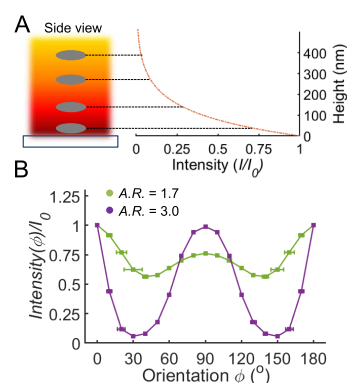

Figure 5. Effect of the particle position and orientation in the scattering intensity under TIRM illumination. (A) Scattering intensity under evanescent wave illumination as a function of particle−substrate separation distance. (B) Scattering intensity as a function of the particle azimuthal orientation ϕ for ellipsoids of AR = 1.7 and 3.0 at a fixed height. The scattering intensity is normalized for $\phi = 0°$, at which the scattering morphology has the most symmetry.

intensity I_0 at the minimum height as is typically done in TIRM measurements.

In addition to changes in the particle−surface separation distance, the azimuthal orientation ϕ also affects the scattering intensity of ellipsoidal particles. Figure 5B shows the simulated integrated intensity for ellipsoids AR = 1.7 and 3.0 for a range of ϕ between 0 and $180°$ at a fixed height (0.1 μm). Here, the intensity is shown relative to the value at $\phi = 0°$, which is where the scattering morphology has the largest symmetry. These results show the extent to which intensity changes as a function of the azimuthal orientation of the particle. Figure S6 shows the simulated scattering images for an ellipsoid of AR = 3.0 with the same intensity scale to further highlight the differences in scattering intensity as a function of ϕ. In an experiment with a diffusing ellipsoid, this relationship can be used to decouple the scattering intensity due to changes in the particle azimuthal orientation ϕ from those due to changes in particle height h. For instance, for the ellipsoid with AR = 1.7, the integrated scattering intensity decreases almost by a factor of $\sim$1.8 at $\phi = 40$ and $140°$, which would be otherwise interpreted as a height change of $\sim$60 nm from the minimum distance. Moreover, for the ellipsoid with AR = 3.0, the changes in intensity as a result of ϕ are more pronounced. For these high-aspect-ratio particles, the intensity decreases 16-fold for $\phi = 30$ and $150°$, which would be wrongly interpreted as a height change of $\sim$300 nm from the minimum distance. This partly explains why only a limited range of ϕ between 60 and $120°$ was observed in the experiment for these high-aspect-ratio ellipsoids (Figure 2), as the decrease in intensity (inside this range of ϕ) is only expected to be a factor of $\sim$2, but dimmer particles (outside this range of ϕ) were likely below the detection limit under the experimental conditions used. These observations confirm the sensitivity of the integrated scattered light to changes in ϕ and further point out that ellipsoids with higher AR scatter with a more sensitive dependence on orientation.

Finally, we evaluated the impact of a small variation in the polar angle θ on the integrated scattering intensity of an ellipsoidal particle. These variations could happen during particle deposition and, as explained previously, would be hard to detect using the trigonometric projection of a bright-field image from the top of the sample. Figure 6A shows a side-view
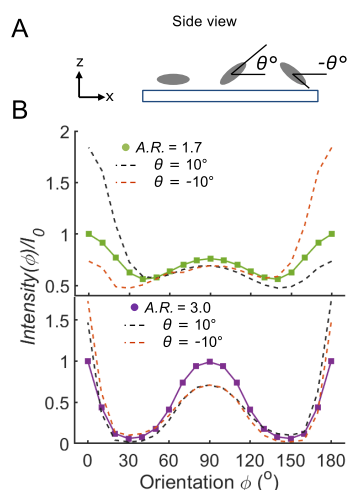
Figure 6. Effect of a small tilt in the particle polar angle θ in the scattering intensity under TIRM illumination. (A) Schematic showing a side view of an ellipsoidal particle and the substrate for $\theta = 0°$ and for variations of $\pm\theta$. (B) Plots of the scattering intensity as a function of ϕ for $\theta = 0, 10,$ and $-10°$, at a fixed height, for ellipsoids of AR = 1.7 (top panel) and 3.0 (bottom panel). For both panels, the intensities are normalized to the scattering intensity at $[\phi, \theta] = [0, 0°]$.

schematic of an ellipsoid aligned with the substrate plane ($\theta = 0°$) and with exaggerated tilts of $\pm\theta$. Similarly to Figure 5B, the scattering intensity was simulated at a constant height of 0.1 μm, measured from the top of the substrate to the lower edge of the particle.

Small changes in the polar angle θ of ellipsoidal particles cause large variations in the scattering intensity under an evanescent field. Figure 6B shows the integrated intensity as a function of ϕ for $\theta = 0, 10,$ and $-10°$ for ellipsoids of AR = 1.7 (top panel) and 3.0 (bottom panel). Similarly to Figure 5B, the intensity here is shown relative to the value at $\phi = 0°, \theta = 0°$, which is when the scattering morphology shows the largest symmetry. For $\theta = 10$ and $-10°$, the intensity as a function of ϕ is no longer mirror-symmetric at 90° (i.e., $I(\phi = 45)° \neq I(\phi = 135)°$), as is the case when $\theta = 0°$. Interestingly, the low AR particles show their larger sensitivity to θ between $0° < \phi < 30$ and $150° < \phi < 180°$, where the intensity increases (or decreases) almost by a factor of ~ 2, depending on θ. For the case of the high AR particles, the integrated intensity increases by a factor of ~ 1.5 around $\phi = 0°$ and decreases by a similar amount around $\phi = 90°$, without losing much of the pronounced sensitivity shown in Figure 5 around $\phi = 30$ and 150°. These simulations thus show that unlike to what was observed for rotations in ϕ, where high AR particles showed higher sensitivity, the low AR ellipsoids scatter more sensitively in response to small variations in θ. Overall, these results also confirm the importance of knowing the particle orientation to deconvolute its effect in the scattering intensity in an evanescent field. In the future, we aim to explore the effect of small variations in particle size in the scattering intensity of ellipsoidal particles, as size-dependent resonances have been reported for spherical particles in the Mie regime.[41]

These data, taken together with the data summarized above, provide a pathway by which each of the orientation angles and separation distance of an ellipsoidal particle can be uniquely obtained, thereby decoupling contributions to the scattering intensity to be used for an SMR-TIRM experiment. The

morphology angle M_ϕ, as it is sensitive to the azimuthal angle but not polar angle, should first be used to determine the azimuthal orientation of the particle (see Figures 2 and 3). Subsequently, the morphology aspect ratio M_{AR} should be used at a given azimuthal angle to determine variations in the polar angle of the particle (see Figure 4). Once both the azimuthal and polar angles are known, these values can be used to correct for variations in integrated intensity via the known relationships between relative integrated intensity and angle (see Figures 5 and 6). Finally, the corrected integrated intensity would be used for a unique determination of separation distance. We propose this path for conducting SMR-TIRM to obtain potential energy landscapes based on the data presented herein, with ongoing work to test this protocol.

■ CONCLUSIONS

The initial development of scattering morphology resolved total internal reflection (SMR-TIRM) was described herein. Central to the development of this technique is the hypothesis that the morphology of light scattered from a colloidal ellipsoid is a sensitive function of orientation. The hypothesis was tested via combined experimental and computational mapping of scattered light morphology from colloidal ellipsoids at a fixed separation distance and orientation. Morphologies were parameterized with the orientation M_ϕ and aspect ratio M_{AR} of the fitted 2D Gaussian surface. The azimuthal orientation was predicted from a simulated relation between M_ϕ and ϕ. When conducted with experimental data and simulated data, this exercise yielded results that were comparable or better in accuracy than the angular resolution in ϕ expected from bright-field microscopy. Further, simulated mapping results revealed the exquisite sensitivity of M_{AR} to the polar angle. Such sensitivity to variations in the polar angle is beyond the angular resolution in θ of a bright-field image also acquired from the top of the sample, taking into account the diffraction limit of light. In conclusion, the morphology of the scattered light was found to be a sensitive function of particle orientation, which causes variations in the scattered light intensity comparable in magnitude to those resulting from fluctuations in separation distance in a conventional TIRM experiment.

■ ASSOCIATED CONTENT

ⓢ Supporting Information

The Supporting Information is available free of charge at https://pubs.acs.org/doi/10.1021/acs.langmuir.0c02482.

> Preparation method; SEM images and size distribution of the ellipsoidal particles used in this study; table containing the input parameters for the simulations; additional experimental bright-field and TIRM images of ellipsoids with AR = 3.0, along with line sections of the scattering intensity; calculations of the uncertainty in the measurement of azimuthal and polar angles from bright-field images; M_{AR} as a function of θ for different ϕ; simulated TIRM images as a function of ϕ shown with the same intensity grayscale; and tables showing the relative changes in M_{AR} for $\Delta\theta = 10°$ (PDF)

■ AUTHOR INFORMATION

Corresponding Author

Christopher L. Wirth − *Chemical and Biomolecular Engineering Department, Case Western Reserve University,*

Cleveland, Ohio 44106, United States; ⊚ orcid.org/0000-0003-3380-2029; Email: wirth@case.edu

Authors

Aidin Rashidi − *Chemical and Biomolecular Engineering Department, Case Western Reserve University, Cleveland, Ohio 44106, United States*

Sergio Domínguez-Medina − *Chemical and Biomolecular Engineering Department, Case Western Reserve University, Cleveland, Ohio 44106, United States;* ⊚ orcid.org/0000-0002-0463-8488

Jiarui Yan − *Chemical and Biomedical Engineering, Cleveland State University, Cleveland, Ohio 44115, United States*

Dmitry S. Efremenko − *Remote Sensing Technology Institute (IMF), German Aerospace Center (DLR), 82234 Oberpfaffenhofen, Germany*

Alina A. Vasilyeva − *Faculty of Electrical Engineering and Information Technology, University of Applied Sciences, 83024 Rosenheim, Germany*

Adrian Doicu − *Remote Sensing Technology Institute (IMF), German Aerospace Center (DLR), 82234 Oberpfaffenhofen, Germany*

Thomas Wriedt − *Leibniz-Institut für Werkstofforientierte Technologien—IWT, University of Bremen, 28359 Bremen, Germany*

Complete contact information is available at:
https://pubs.acs.org/10.1021/acs.langmuir.0c02482

Author Contributions

[#]A.R. and S.D.-M. contributed equally to this work.

Notes

The authors declare no competing financial interest.

■ REFERENCES

(1) Bevan, M. A.; Eichmann, S. L. Optical Microscopy Measurements of KT-Scale Colloidal Interactions. *Curr. Opin. Colloid Interface Sci.* **2011**, *16*, 149−157.

(2) Likos, C. N. Effective Interactions in Soft Condensed Matter Physics. *Phys. Rep.* **2001**, *348*, 267−439.

(3) Trefalt, G.; Palberg, T.; Borkovec, M. Forces between Colloidal Particles in Aqueous Solutions Containing Monovalent and Multivalent Ions. *Curr. Opin. Colloid Interface Sci.* **2017**, *27*, 9−17.

(4) Shrestha, S.; Wang, B.; Dutta, P. Nanoparticle Processing: Understanding and Controlling Aggregation. *Adv. Colloid Interface Sci.* **2020**, *279*, No. 102162.

(5) Kleshchanok, D.; Tuinier, R.; Lang, P. R. Direct Measurements of Polymer-Induced Forces. *J. Phys.: Condens. Matter* **2008**, *20*, No. 073101.

(6) Butt, H.-J.; Cappella, B.; Kappl, M. Force Measurements with the Atomic Force Microscope: Technique, Interpretation and Applications. *Surf. Sci. Rep.* **2005**, *59*, 1−152.

(7) Bos, R.; van der Mei, H. C.; Busscher, H. J. Physico-Chemistry of Initial Microbial Adhesive Interactions − Its Mechanisms and Methods for Study. *FEMS Microbiol. Rev.* **1999**, *23*, 179−230.

(8) Yuan, C.; Quinn, E.; Kucukal, E.; Kapoor, S.; Gurkan, U. A.; Little, J. A. Priapism, Hemoglobin Desaturation, and Red Blood Cell Adhesion in Men with Sickle Cell Anemia. *Blood Cells, Mol., Dis.* **2019**, *79*, No. 102350.

(9) Israelachvili, J.; Min, Y.; Akbulut, M.; Alig, A.; Carver, G.; Greene, W.; Kristiansen, K.; Meyer, E.; Pesika, N.; Rosenberg, K.;

(10) Butt, H.-J.; Cappella, B.; Kappl, M. Force Measurements with the Atomic Force Microscope: Technique, Interpretation and Applications. *Surf. Sci. Rep.* **2005**, *59*, 1−152.

(11) Prieve, D. C. Measurement of Colloidal Forces with TIRM. *Adv. Colloid Interface Sci.* **1999**, *82*, 93−125.

(12) Prieve, D. C.; Walz, J. Y. Scattering of an Evanescent Surface Wave by a Microscopic Dielectric Sphere. *Appl. Opt.* **1993**, *32*, 1629−1641.

(13) Biggs, S.; Prieve, D. C.; Dagastine, R. R. Direct Comparison of Atomic Force Microscopic and Total Internal Reflection Microscopic Measurements in the Presence of Nonadsorbing Polyelectrolytes. *Langmuir* **2005**, *21*, 5421−5428.

(14) Nayeri, M.; Abbas, Z.; Bergenholtz, J. Measurements of Screening Length in Salt Solutions by Total Internal Reflection Microscopy: Influence of van Der Waals Forces and Instrumental Noise. *Colloids Surf., A* **2013**, *429*, 74−81.

(15) Ao, Z.; Liu, G.; Zhang, G. Ion Specificity at Low Salt Concentrations Investigated with Total Internal Reflection Microscopy. *J. Phys. Chem. C* **2011**, *115*, 2284−2289.

(16) Nellen, U.; Dietrich, J.; Helden, L.; Chodankar, S.; Nygård, K.; Friso van der Veen, J.; Bechinger, C. Salt-Induced Changes of Colloidal Interactions in Critical Mixtures. *Soft Matter* **2011**, *7*, No. 5360.

(17) Bevan, M. A.; Prieve, D. C. Direct Measurement of Retarded van Der Waals Attraction. *Langmuir* **1999**, *15*, 7925−7936.

(18) Bevan, M. A.; Prieve, D. C. Hindered Diffusion of Colloidal Particles Very near to a Wall: Revisited. *J. Chem. Phys.* **2000**, *113*, 1228−1236.

(19) Wirth, C. L.; Rock, R. M.; Sides, P. J.; Prieve, D. C. Single and Pairwise Motion of Particles near an Ideally Polarizable Electrode. *Langmuir* **2011**, *27*, 9781−9791.

(20) Wirth, C. L.; Sides, P. J.; Prieve, D. C. Electrolyte Dependence of Particle Motion near an Electrode during Ac Polarization. *Phys. Rev. E* **2013**, *87*, No. 032302.

(21) Wu, H.-J.; Bevan, M. A. Direct Measurement of Single and Ensemble Average Particle−Surface Potential Energy Profiles. *Langmuir* **2005**, *21*, 1244−1254.

(22) Wu, H.; Pangburn, T. O.; Beckham, R. E.; Bevan, M. A. Measurement and Interpretation of Particle−Particle and Particle−Wall Interactions in Levitated Colloidal Ensembles. *Langmuir* **2005**, *21*, 9879−9888.

(23) Besseling, T. H.; Hermes, M.; Kuijk, A.; De Nijs, B.; Deng, T. S.; Dijkstra, M.; Imhof, A.; Van Blaaderen, A. Determination of the Positions and Orientations of Concentrated Rod-like Colloids from 3D Microscopy Data. *J. Phys.: Condens. Matter* **2015**, *27*, No. 194109.

(24) Xiao, L.; Ha, J. W.; Wei, L.; Wang, G.; Fang, N. Determining the Full Three-Dimensional Orientation of Single Anisotropic Nanoparticles by Differential Interference Contrast Microscopy. *Angew. Chem., Int. Ed.* **2012**, *51*, 7734−7738.

(25) Marchuk, K.; Fang, N. Three-Dimensional Orientation Determination of Stationary Anisotropic Nanoparticles with Sub-Degree Precision under Total Internal Reflection Scattering Microscopy. *Nano Lett.* **2013**, *13*, 5414−5419.

(26) Lee, J.; Kim, G. W.; Ha, J. W. Single-Particle Spectroscopy and Defocused Imaging of Anisotropic Gold Nanorods by Total Internal Reflection Scattering Microscopy. *Analyst* **2020**, *145*, 6038−6044.

(27) Jiang, Y.; Su, H.; Wei, W.; Wang, Y.; Chen, H. Y.; Wang, W. Tracking the Rotation of Single CdS Nanorods during Photocatalysis with Surface Plasmon Resonance Microscopy. *Proc. Natl. Acad. Sci. U.S.A.* **2019**, *116*, 6630−6634.

(28) Glotzer, S. C.; Solomon, M. J. Anisotropy of Building Blocks and Their Assembly into Complex Structures. *Nat. Mater.* **2007**, *6*, 557−562.

(29) Eichmann, S. L.; Smith, B.; Meric, G.; Fairbrother, D. H.; Bevan, M. A. Imaging Carbon Nanotube Interactions, Diffusion, and Stability in Nanopores. *ACS Nano* **2011**, *5*, 5909−5919.

Zeng, H. Recent Advances in the Surface Forces Apparatus (SFA) Technique. *Rep. Prog. Phys.* **2010**, *73*, No. 036601.

(30) Rashidi, A.; Razavi, S.; Wirth, C. L. Influence of Cap Weight on the Motion of a Janus Particle Very near a Wall. *Phys. Rev. E* **2020**, *101*, 1−9.

(31) Doicu, A.; Vasilyeva, A. A.; Efremenko, D. S.; Wirth, C. L.; Wriedt, T. A Light Scattering Model for Total Internal Reflection Microscopy of Geometrically Anisotropic Particles. *J. Mod. Opt.* **2019**, *66*, 1139−1151.

(32) Ho, C. C.; Keller, A.; Odell, J. A.; Ottewill, R. Preparation of Monodisperse Ellipsoidal Polystyrene Particles. *Colloid Polym. Sci.* **1993**, *271*, 469−479.

(33) Doicu, A.; Köser, J.; Wriedt, T.; Bauckhage, K. Light Scattering Simulation and Measurement of Monodisperse Spheroids Using a Phase Doppler Anemometer. *Part. Part. Syst. Charact.* **1998**, *15*, 257−262.

(34) Helden, L.; Eremina, E.; Riefler, N.; Hertlein, C.; Bechinger, C.; Eremin, Y.; Wriedt, T. Single-Particle Evanescent Light Scattering Simulations for Total Internal Reflection Microscopy. *Appl. Opt.* **2006**, *45*, No. 7299.

(35) Waterman, P. C. Symmetry, Unitarity, and Geometry in Electromagnetic Scattering. *Phys. Rev. D* **1971**, *3*, 825−839.

(36) Waterman, P. C. Matrix Formulation of Electromagnetic Scattering. *Proc. IEEE* **1965**, *53*, 805−812.

(37) Wolf, E. Electromagnetic Diffraction in Optical Systems - I. An Integral Representation of the Image Field. *Proc. R. Soc. A* **1959**, *253*, 349−357.

(38) Doicu, A.; Wriedt, T.; Eremin, Y. A. *Light Scattering by Systems of Particles*, 1st ed.; Springer Series in OPTICAL SCIENCES; Springer Berlin Heidelberg: Berlin, Heidelberg, 2006; *Vol. 124*.

(39) Doicu, A.; Wriedt, T.; Eremin, Y. The Null-field Method with Discrete Sources is an extension of the Null-field Method (also called T-Matrix Method) to compute light scattering by arbitrarily shaped dielectric particles, 2006. Scattport. https://scattport.org/index.php/programs-menu/t-matrix-codes-menu/239-nfm-ds (accessed October 1, 2020).

(40) Nootz, G. Fit 2D Gaussian Function to Data, 2012. MATLAB Central File Exchange. https://www.mathworks.com/matlabcentral/fileexchange/37087-fit-2d-gaussian-function-to-data (accessed October 1, 2020).

(41) Mishchenko, M. I.; Lacis, A. A. Manifestations of Morphology-Dependent Resonances in Mie Scattering Matrices. *Appl. Math. Comput.* **2000**, *116*, 167−179.